aerospace

MDPI

Article

Improvement in Efficiency of Blunt Cone Drag and Heat Reduction by Combination of Aerospike and Partition Jets

Shuang Wang, Yongkang Zheng, Hao Tian and Zhigong Tang *

China Aerodynamics Research and Development Center, Mianyang 621000, China; ws119348@163.com (S.W.)
* Correspondence: tangzhigong@126.com

Abstract

To mitigate the severe aerodynamic and thermal loads on high-speed vehicles, a combined control approach employing an aerospike and a partition jet system is investigated. The influence of jet position on flow field behavior, drag reduction and thermal load management is examined. Using the SST k-ω turbulence model integrated into a finite-volume framework, the study conducts numerical simulations by solving the three-dimensional Reynolds-averaged Navier–Stokes equations at a flight altitude of 30 km and Mach 5. Considering that the reverse force generated by the top and bottom jets would cause an increase in drag along the direction of motion, the lateral jet contributes more significantly to the drag reduction. The combination of the aerospike and multi-zone jets performs better in terms of drag reduction and thermal protection than single-zone jet strategies. Among them, the scheme with simultaneous jets at three positions has the highest drag reduction efficiency, up to 230%, but it requires the most working medium. Through the comprehensive analysis of the heat and drag reduction efficiency, the lateral jet is the optimal configuration.

Keywords: high-speed vehicles; aerospike; partition jet; drag and heat flux reduction; numerical simulation

1. Introduction

For modern high-speed vehicle development, velocity has emerged as a critical design parameter to achieve time-sensitive operational objectives [1]. The increase in flight speed inevitably leads to increased aerodynamic drag and heat. High drag could affect the maneuverability [2,3], while intense heating requires the vehicles to be equipped with thermal protection systems, which increases launch costs and decreases the effective payload [4]. Thus, the reduction in aerodynamic drag and heat flux is highly significant for the design of high-speed flight vehicles.

In high-speed flows, the nose and fuselage leading edge typically endure the most intense thermal loads. Simultaneously, the nose's geometry governs the shock wave's morphology, directly influencing drag coefficients. To actively manage drag and heat flux, researchers have explored diverse flow control methods aimed at restructuring the flow field [5,6]. The forward-facing cavity [7], energy deposition [8,9], installation of aerospike [10], transpiration cooling [11–13], counter-flowing jets [14,15], etc., are all commonly employed drag reduction schemes based on flow field control. The aerospike, due to its simple structure and remarkable drag reduction effect, has gained the preference of numerous researchers. By piercing the powerful shock generated at high Mach numbers,

Check for updates

Academic Editor: Bosko Rasuo

Received: 15 January 2026
Revised: 25 February 2026
Accepted: 27 February 2026
Published: 3 March 2026

Copyright: © 2026 by the authors. Licensee MDPI, Basel, Switzerland. This article is an open access article distributed under the terms and conditions of the Creative Commons Attribution (CC BY) license.

the spike transforms it into an oblique shock, markedly reducing drag. However, its thermal protection remains inadequate, and aerodynamic performance declines noticeably at non-zero angles of attack, limiting its practical application.

To attain satisfactory overall drag reduction and thermal protection, combined flow control schemes integrating active thermal protection with passive flow control have emerged in recent years. Jiang et al. [16,17] introduced an innovative configuration combining spike with lateral jet systems, conducting comprehensive experimental and computational analyses. Their findings revealed that lateral jets effectively pushed away the reattachment shock waves and diminished shock intensity. Guo et al. [18] further studied a dual-configuration system incorporating a spike-aerodisk with specially designed airflow channels. This design enables high-pressure air captured behind bow shocks to enter through aerodisk channels, subsequently expelled through lateral jets along the spike body for simultaneous aerodynamic and thermal mitigation. Liu et al. [19] engineered a three-part system incorporating spike-aerodisks with lateral and rear jet mechanisms to enhance high-speed vehicle performance. Their findings reveal substantial reductions in drag coefficient and improved thermal protection efficacy via synchronized jet operation. Ou et al. [20] performed configuration optimization on integrated spike and counterflow jet setups using numerical simulation paired with multi-objective evolutionary algorithms under high-speed flow conditions at Mach 5.75. Their research framework established dual optimization objectives encompassing both the comprehensive drag coefficient and thermal load distribution characteristics at the leading edge of blunt-nosed structures. Although current studies have addressed the jet effects of single-position or multi-position, there remains a notable lack of systematic research on the simultaneous implementation of multi-zone synergistic jets, specifically at the top, lateral and bottom, on the aerospike. In particular, the coupling mechanism of multi-jet interfering with the flow field and its influence on the drag and heat flux reduction efficiency are still unclear.

Based on this, the paper processes a combined drag and heat flux reduction scheme integrating an aerospike with partition jets. The effects of top, lateral and bottom jets and their combinations on flow field structure, as well as wall pressure and heat distributions, are systematically analyzed. The law of shock shape and separation zone evolution caused by multi-jet interference is revealed. The drag reduction and thermal protection efficiency of each scheme are evaluated.

2. Physical Models and Numerical Methods

2.1. Physical Model

The combined aerospike–partition jet configuration is shown in Figure 1. The configuration consists of a combination of a spike and a blunt cone, with the axis of the spike and the center of the blunt body aligned on the x-axis. The blunt cone has a nose radius of 27.94 mm, and its conical section forms an angle of 15° with the positive direction of the x-axis, with a total length of 447.04 mm. The spike, measuring 250 mm in length and 25 mm in diameter, is installed along the axis of the blunt cone nose. A top nozzle is located at the tip of the spike, featuring a circular orifice with a diameter of 6 mm, centered on the x-axis, with the jet directed along the negative x-axis. A lateral nozzle is positioned at the midpoint of the spike, configured as an annular slot with a width of 2 mm, and the jet direction is perpendicular to the x-axis. The angle between the normal direction of the blunt body surface and the negative x-axis is denoted by θ. The bottom nozzle is an annular slot with a width of 2 mm, with its center line positioned along the $\theta = 45°$ contour line of the blunt body, and the jet direction is perpendicular to the blunt body wall. The three nozzles could be activated as needed; when not in operation, the jet orifices function as regular wall surfaces, indistinguishable from the rest of the spike and the blunt cone

surface. The blue arrows in Figure 1 indicate the direction of the jet. The configuration is axisymmetric, and a three-dimensional half model is adopted to conserve computational resources. Figure 2 illustrates the computational structured grid.

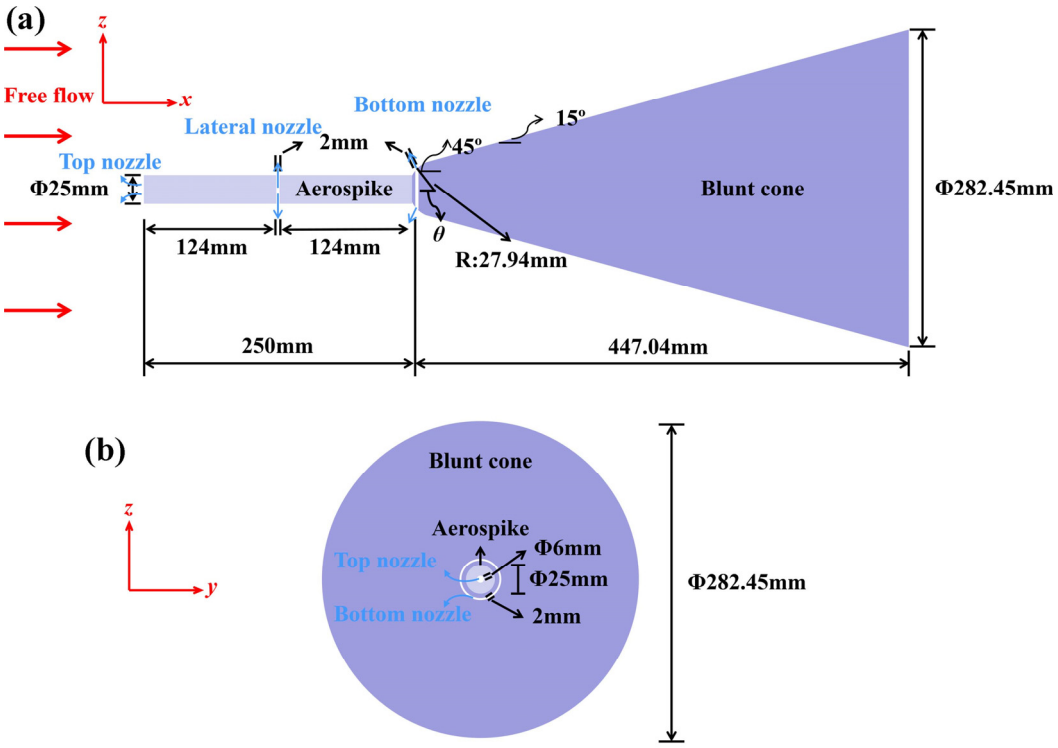


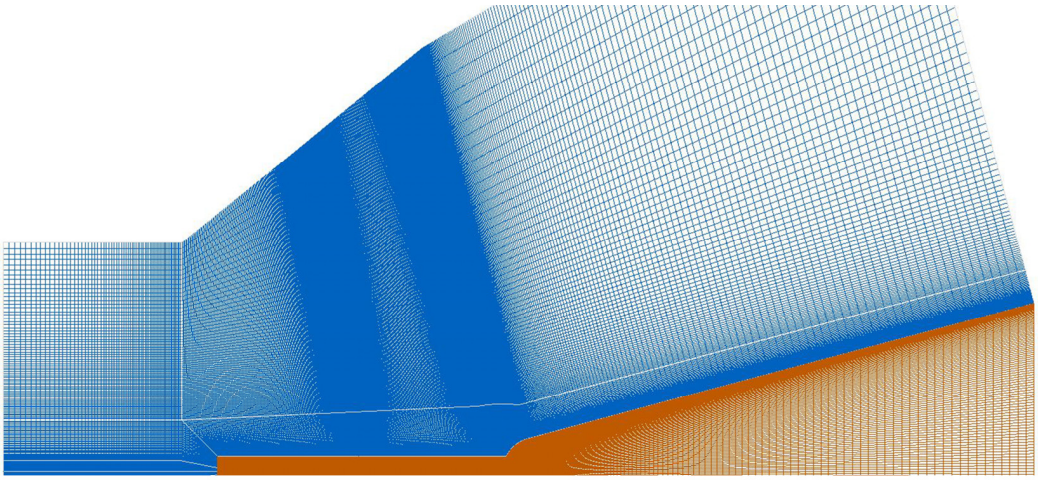
Figure 1. Schematic representation of the physical model: (**a**) in the xz plane and (**b**) in the yz plane.

Multiple multi-zone jet configurations, illustrated in Figure 3, are investigated and compared. Cases 001–004 focus on the influence of spike–single-zone jet configuration on drag and heat reduction of the models; Cases 005–007 explore combinations of two jet modes; and Case 008 analyzes the simultaneous use of jets at all three locations. In addition, the jet efficiency of the work medium in Cases 002–008 also needs to be considered.

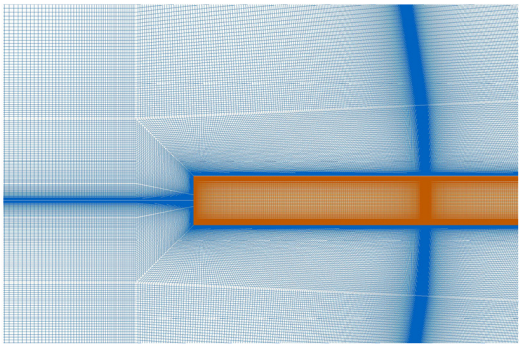
The flight altitude of 30 km and the Mach number of 5 are selected as the freestream condition. The far field of the computational domain is set as the pressure far-field boundary condition. The outlet is set as the pressure outlet boundary condition. The wall of the geometric model adopts the no-slip isothermal boundary condition, and the wall temperature T_w is 300 K. Both the main flow and the jet flow media are air. The jet temperature is set as 300 K, and the jet-to-freestream total pressure ratio is 0.1.

2.2. Numerical Approaches

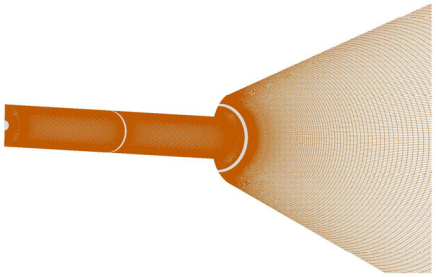
The three-dimensional, steady-state Reynolds-Averaged Navier–Stokes (RANS) equations are solved in conjunction with the SST k-ω turbulence model. The solver employed is based on double precision, density-based and implicit schemes. The Roe flux scheme based on the Muller-type entropy correction method is utilized for spatial discretization, and time advance is made by the data parallel line relaxation method. The air is assumed to follow the ideal gas model, and the air viscosity is determined using the Sutherland viscosity law. Thermal conditions remain below 2500 K, precluding consideration of chemical reaction mechanisms. In this paper, the flow field is steady, and the convergence criterion is that all residuals are less than 1×10^{-5}.



(a) Mesh on the symmetrical plane



(b) Mesh near the aerospike



(c) Mesh on the body surface

Figure 2. Computational structured grids on the surface and symmetrical plane.

2.3. Grid Independence Analysis

The accuracy of wall heat flux calculations is highly dependent on mesh quality. Additionally, the SST *k-ω* turbulence model requires particular mesh resolution standards to guarantee reliable solutions. For grid independence verification, a blunt cone configuration is analyzed across three distinct grid resolutions, with comprehensive specifications documented in Table 1. The Re_{grid} is defined as $\rho U \Delta / \mu$, where Δ is the characteristic mesh size in the near-wall region, and ρ, U and μ are the freestream density, velocity and dynamic viscosity, respectively.

Table 1. Three kinds of grid in detail.

Grid Size	First Layer Grid Height/10^{-6} m	Total Grid	Re_{grid}
Coarse mesh	26.43176	4,720,677	20
Moderate mesh	5.286532	6,318,000	10
Refined mesh	2.643176	8,853,004	5

The pressure coefficient Cp is defined as follows:

$$Cp = \frac{p - p_\infty}{1/2 \rho_\infty v_\infty^2} \quad (1)$$

where p is the surface pressure, p_∞, ρ_∞ and v_∞ are the free stream pressure, density and velocity, respectively. Results for the Cp and heat flux density (q), derived from computations across three grid types, are illustrated in Figure 4. The Cp distributions

demonstrate lower grid sensitivity compared to heat flux variations, with all three grid types producing almost identical pressure coefficient patterns, as evidenced in Figure 4a. The calculation results of coarse mesh have more deviation from moderate mesh and refined mesh. While the moderate and refined grids show strong agreement in most regions, a notable discrepancy emerges in heat flux density calculations near the x = 0.1 coordinate. Considering the balance between computational resource conservation and result precision, the moderate grid configuration was ultimately selected for subsequent analyses.

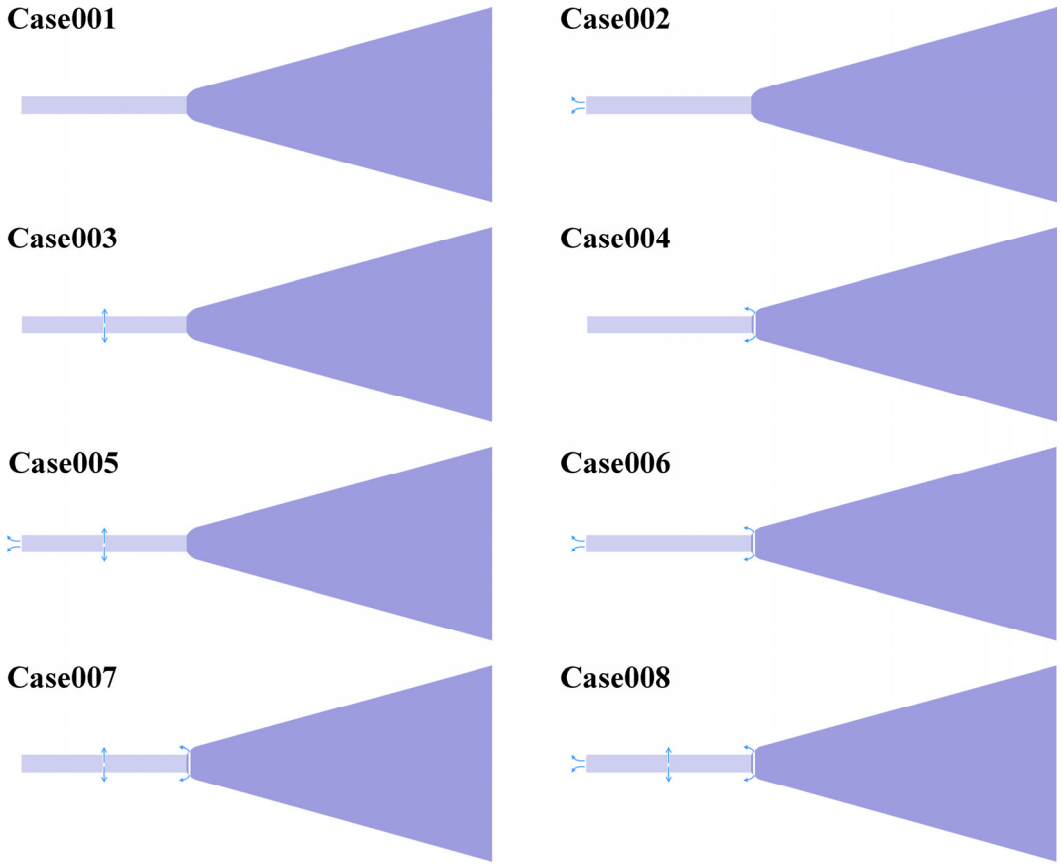


Figure 3. Schematics of the simulated cases.

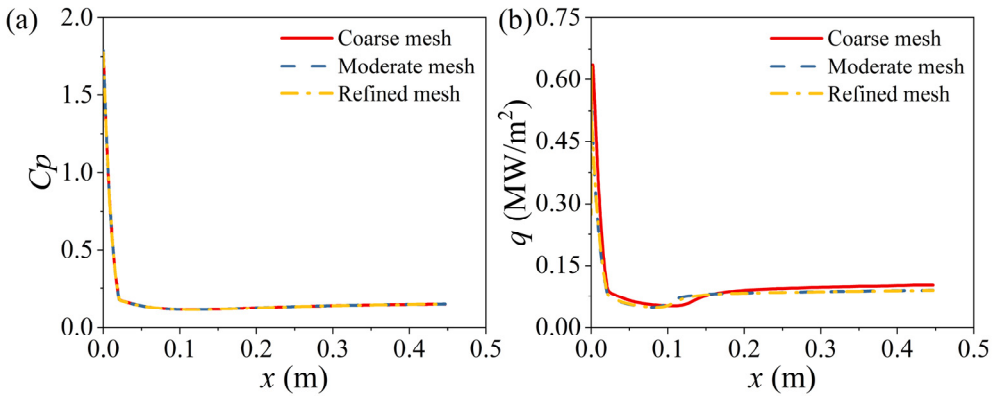


Figure 4. (**a**) Wall pressure coefficient and (**b**) heat flux distribution along the axis of blunt cone symmetry.

2.4. Code Validation

The structures under investigation include a spike and a blunt cone with jet flow. Its flow field structure is complex, including flow separation and reattachment, shock wave

interaction and other complex flow phenomena, so it is necessary to perform numerical verification for those flow features. To assess the numerical method's reliability, validation is performed on a blunt cone equipped with counter-jet flows. The model for numerical analysis is designed for comparison purposes to be identical to Hayashi [21]. The test specimen features a 50 mm-diameter hemispherical base with a 4 mm-diameter perpendicular injection port aligned along the central axis. The wind tunnel testing parameters include Mach 8 freestream velocity, 4.50 MPa stagnation pressure ($p_{0\infty}$), 800 K total temperature and zero angle of attack. Both the freestream and jet flows utilize atmospheric air, with the nozzle operating at Mach 1.5 relative to incoming flow. The jet-to-freestream total pressure ratios (PR = $p_{0j}/p_{0\infty}$) are set at 0.0251 and 0.0859, respectively, under a constant wall temperature of 300 K.

Figure 5 displays a comparison of experimental schlieren images and computed density distributions across varying pressure ratios. As illustrated, the numerical results accurately reproduce key flow features, including the Mach disk, jet bow shock and triple-wave point. At PR = 0.0251, interaction between the free stream and reverse jet produces a bow shock and a reattachment shock near the hemisphere's shoulder. Raising the pressure ratio to PR = 0.0859 leads to substantial alterations in the flow, characterized by forward movement of shock structures and disappearance of reattachment. Additionally, Figure 6 provides a comparison of surface pressure distributions along the hemisphere. The ϕ is the angle measured from the stagnation point around the center of the hemisphere, and the pressure data are normalized by the freestream pressure. The numerical predictions under different pressure ratios align closely with experimental measurements, demonstrating excellent agreement. The computational approach employed in this study exhibits high accuracy and effectively simulates jet interaction flow fields in high-speed conditions.

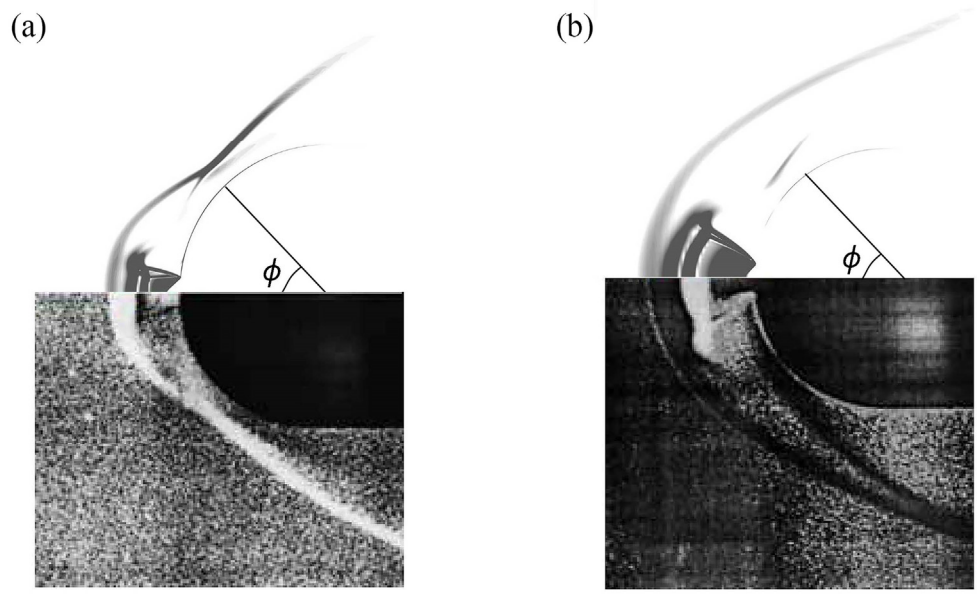


Figure 5. Comparison of the experimental schlieren image and computed density field at (**a**) PR = 0.0251 and (**b**) PR = 0.0859 (the experimental figures are reprinted with permission from Ref. [21]. 2006, Hayashi).

The available high-speed drag-reducing disk-wrapped flow test is selected as the verification example [22]. The experimental configuration features a hemispherical body with a 40 mm diameter, coupled with a 5 mm diameter spike that extends 40 mm in length and is tipped by a hemispherical aerodisk of 5 mm radius for drag reduction. The freestream is at 7 Mach, with a temperature of 840 K and no angle of attack.

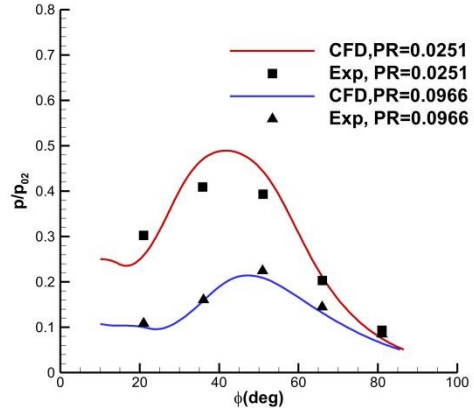


Figure 6. Experimental and simulated pressure distribution along the blunt body surface (the experimental data are reprinted with permission from Ref. [21]. 2006, Hayashi).

Figure 7a contrasts the experimental schlieren image with the computed density field. Numerical simulation accurately captures the bow shock structure ahead of the aerospike. Flow separation occurs at the disk's shoulder, generating a separation shock, while a reattachment shock emerges near the blunt body's shoulder. These shock patterns align closely with schlieren experimental data. Figure 7b displays surface pressure distribution along the blunt body, revealing a pressure peak near its shoulder region, consistent with empirical measurements. This pressure data are normalized by the freestream static pressure and specific heat ratio, and angle ϕ represents the angle from the stagnation point around the center of the hemisphere body. These results confirm the computational model's validity for aerodynamic analysis of the drag reduction spike configuration.

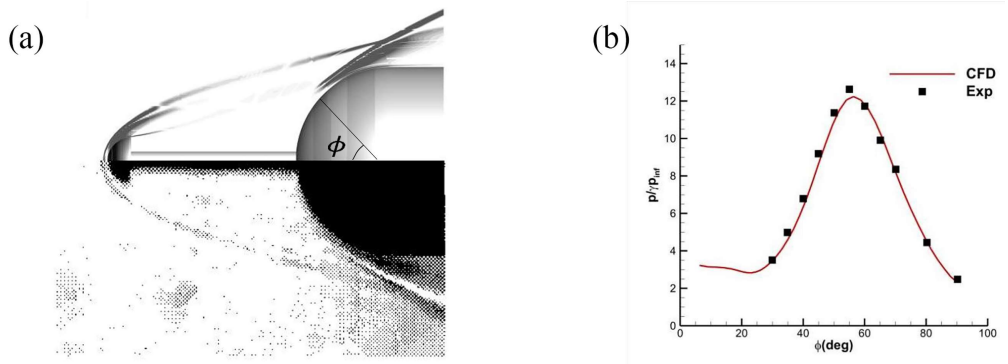


Figure 7. (**a**) Comparison of experimental schlieren and simulated density field and (**b**) comparison of measured and computed surface pressure on the blunt body (the experimental figure and data are reprinted with permission from Ref. [22]. 2001, Motoyama).

3. Results and Discussion

Using the non-jet blunt cone and spike configuration as baseline references, the study first examines the aerodynamic phenomena associated with head-mounted spike configurations under high-speed flight conditions. Subsequently, the flow field characteristics are further examined at different positions of the spike and blunt cone. Finally, an analysis is conducted on the flow field properties of the arrangement featuring partitioned jet flow. Quantitative assessments of jet-induced drag mitigation and thermal protection enhancements are performed.

The Stanton number, St, is used to present the heat flux, defined as Equations (2) and (3):

$$St = \frac{q}{(T_{aw} - T_w)\rho_\infty v_\infty c_p} \quad (2)$$

$$T_{aw} = T_{\infty}\left\{1 + [(\gamma - 1)/2]Ma^2\mathrm{Pr}^{1/3}\right\} \tag{3}$$

where T_{aw} is the adiabatic wall temperature and T_w is the wall temperature. T_{∞}, γ, Ma and Pr are free stream temperature, ratio of specific heats, Mach number and Prandtl number, respectively.

The jet drag reduction efficiency, denoted as η, is introduced to quantify the improvement in drag reduction performance achieved by various jet configurations compared to a reference configuration. It is defined by Equation (4):

$$\eta = \frac{D_1 - D_2}{D_0 - D_1} \times 100\% \tag{4}$$

where D is the drag, and the unit is N. D_0 denotes the drag of the baseline blunt cone without the drag reduction device, D_1 represents the drag of the blunt cone after the addition of the spike, and D_2 corresponds to the drag obtained for the combined configuration. When the angle between the jet direction and the freestream direction is greater than 90°, the drag represented by D_2 includes not only the aerodynamic drag but also the additional drag caused by the reverse action of the jet gas. The specific calculation relationship is shown in Equations (5) and (6):

$$D_2 = D_q + D_{jet} \tag{5}$$

$$D_{jet} = (P_{jet} - P_{\infty} + \rho_{jet}v_{jet}^2)S_{eff} \tag{6}$$

where D_q and D_{jet} are the aerodynamic drag and jet additional drag, respectively. S_{eff} is the projected area of the jet in the free stream direction, P_{jet} and P_{∞} are the jet pressure and free stream pressure, respectively, and v_{jet} is the jet velocity.

The equivalent specific impulse I, defined as the drag reduction per unit mass flow rate of the jet gas, is expressed in units of m/s and is given by:

$$I = \frac{D_0 - D_2}{Q} \tag{7}$$

where Q represents the mass flow rate of the jet in kg/s.

The drag coefficient C_d is defined as:

$$C_d = \frac{D}{1/2\rho_{\infty}v_{\infty}^2} \tag{8}$$

3.1. Characteristics of the Flow Field of Reference Configurations

To examine the influence of jet placement on drag and heat flux reduction and thermal protection performance, the blunt cone (designated as Case 000) and the aerospike-equipped blunt cone (Case 001) are used as baseline configurations. The corresponding flow fields without jet interaction are acquired under identical high-speed freestream conditions. Numerical simulation results depicting Mach number and pressure contours for these reference cases are presented in Figure 8.

As shown in Figure 8, computational results distinctly capture complex flow structures such as the bow shock, shear layer, reattachment shock and recirculation zone. Compression of the high-speed free stream by the blunt cone produces a pronounced bow shock ahead of the nose, resulting in substantial wave drag and affecting the aerodynamics of the high-speed vehicle. Moreover, high-temperature gas within the shock layer transfers extensive thermal energy to the cooler surface of the blunt cone, inducing severe heat flux that introduces considerable operational hazards. Following the installation of an aerospike ahead of the blunt cone, a detached bow shock emerges in the free stream at the tip of the aerospike. Maximum shock intensity occurs near the rod's stagnation region, while

the remaining shock structure predominantly exhibits oblique shock characteristics that minimally perturb the undisturbed free stream flow. Flow separation emerges behind the aerospike, leading to the development of a recirculation region downstream of the separation location. Within this zone, the shear layer interacts with both the aerospike surface and the blunt cone head. The presence of this recirculation zone contributes to the formation of a separation shock wave. As the flow continues downstream, the shear layer impinges upon the surface of the blunt cone, generating a reattachment shock wave. The position where this reattachment shock forms lies in proximity to the shoulder region of the blunt cone. Owing to the substantial angle of the reattachment shock, it is anticipated that the temperature and pressure of the airflow will increase sharply after passing through the shock. This escalation presents considerable challenges for thermal management in the shoulder area of the blunt cone. Furthermore, the upstream separation shock interacts with the reattachment shock in the vicinity of the reattachment point. Analysis based on streamline patterns reveals that the high-temperature gas compressed by the reattachment shock comes into direct contact with the surface of the blunt cone. This condition is highly detrimental to effective thermal protection. Studies in the related literature have shown that the shoulder region of blunt bodies equipped with aerospike configurations may be subjected to thermal conditions more severe than those at the stagnation point, potentially leading to the formation of localized hot spots.

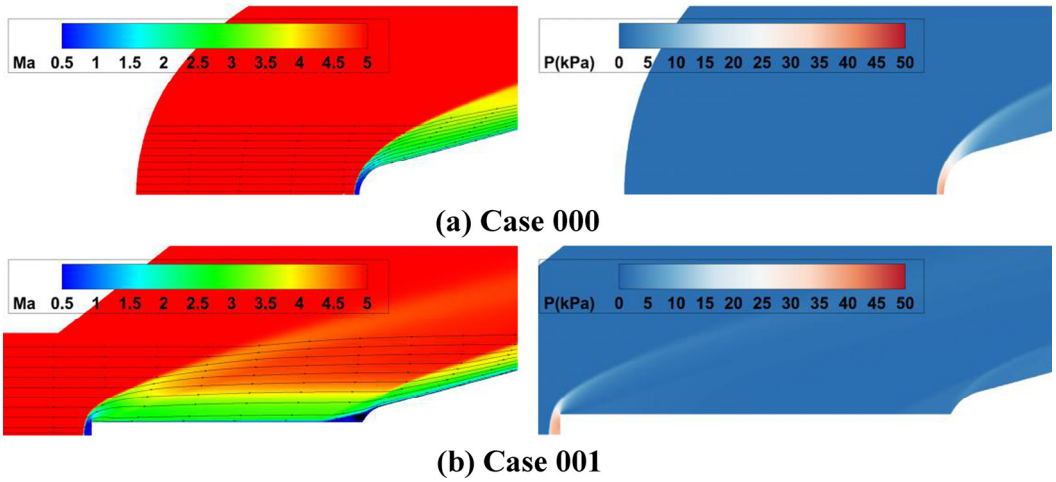


Figure 8. Mach numbers and pressure contours for (**a**) Case 000 and (**b**) Case 001.

Figure 9 displays a comparative analysis of pressure coefficients and Stanton number for Cases 000 and 001. Mounting the aerospike ahead of the blunt cone results in a marked decrease in pressure coefficients across the blunt body, though an elevation is observed near its shoulder. The presence of the spike effectively mitigates aerodynamic heating on the blunt body. Owing to shock wave interactions, more intense aerodynamic heating arises within the shoulder region, leading to an increased Stanton number. These findings regarding both pressure coefficient and Stanton number further corroborate the flow field analysis illustrated in Figure 8.

3.2. Study on the Spike–Single-Zone Jet Configurations

Figure 10 illustrates the flow structure and pressure distribution of the aerospike with a single-zone jet configuration. When a reverse jet is initiated from the tip of the aerospike the shock wave shifts upstream. The jet expands abruptly to supersonic speeds, then decelerates through a Mach disk to subsonic velocities. This ejected flow is deflected and reattaches along the spike's windward side, establishing a recirculation region of low-speed

fluid. It could not only reduce the impact of free flow on the aerospike, but also effectively cool the spike wall to prevent high-temperature ablation. The air attached to the windward surface is separated at the corner of the spike and flows along with the free flow. According to the analysis of the calculation results of Case 002 in Figure 11, *Cp* and Stanton number distributions on the wall of the blunt nose generally show a trend of first rising and then decreasing. When θ is around 25~30°, the wall pressure tends to decrease, but when θ exceeds 30°, the wall pressure of the blunt nose initially rises until attaining peak values at the reattachment point before subsequent decline. The Stanton number also has a similar trend with increasing θ. Comparative analysis of Case 001 data in Figure 9 reveals that enhanced reverse jet flow exerts negligible impact on the distribution trends and values of the Cp and Stanton number.

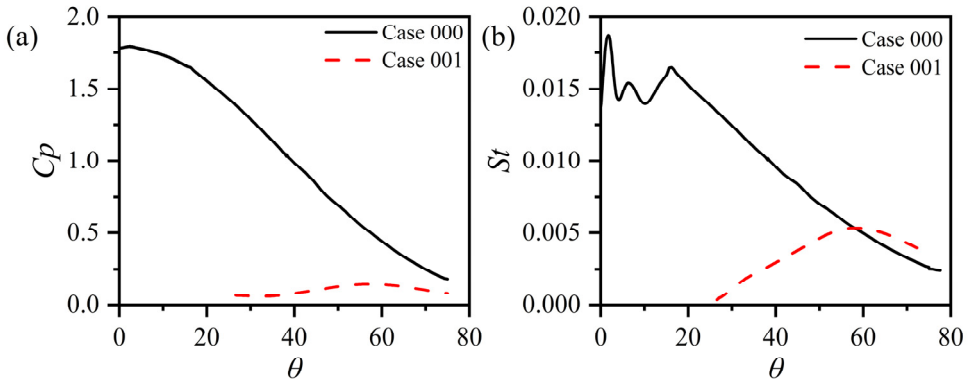


Figure 9. Comparison of (**a**) pressure coefficient and (**b**) Stanton number distributions on the blunt cone.

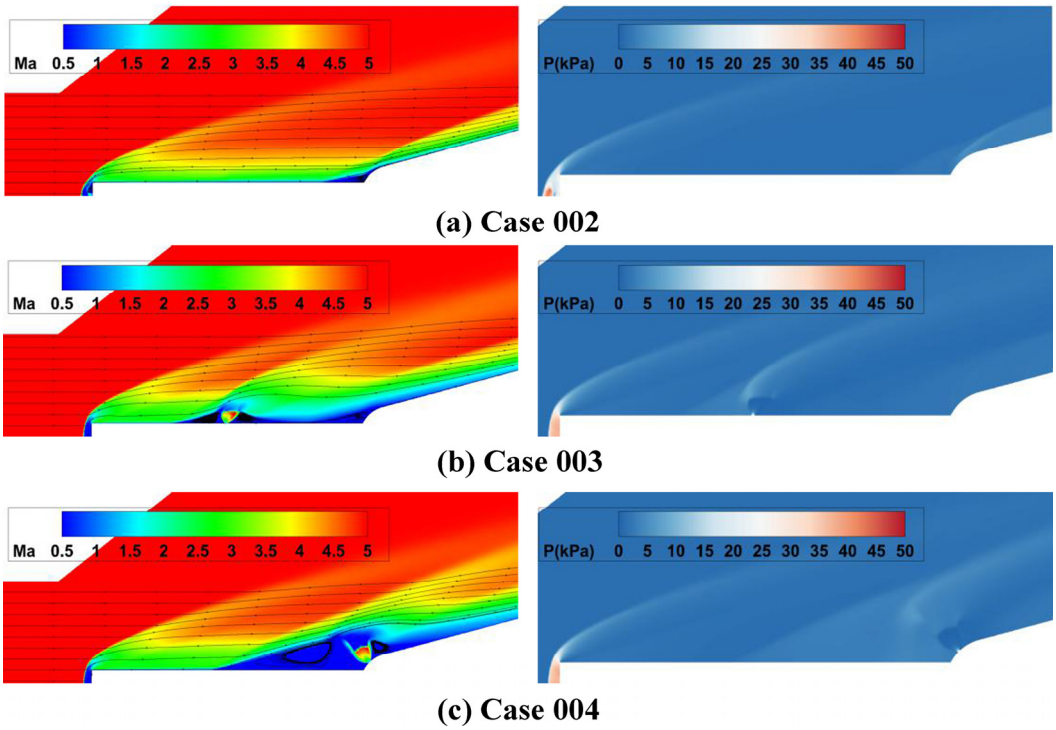


Figure 10. Mach numbers and pressure contours for (**a**) Case 002, (**b**) Case003 and (**c**) Case 004.

After the introduction of the lateral jet, the bow shock generated at the tip of the aerospike is further pushed away. The half angle of shock waves increases significantly, and the distance between the shock wave and the blunt body becomes larger. It is obvious

from Figure 10b that the lateral jet is injected vertically into the high-speed flow and is subjected to the free flow action. While the jet plume demonstrates downstream deflection characteristics, its fundamental under-expanded jet configuration remains identifiable. Recirculation zones are present on each side of the lateral jet nozzle and beneath the aerospike. Introducing the lateral jet leads to a marked expansion of the recirculation zone at the aerospike base, significantly contributing to thermal protection. Cooler jet gas impedes direct interaction between the free stream and the surface, thereby helping mitigate aerodynamic heating. A compression wave generated ahead of the reattachment point compresses near-wall fluid, leading to elevated pressure and thermal gradients in the vicinity of reattachment. This behavior aligns with the tendencies shown in the *Cp* and Stanton number distributions in Figure 11. The trends of the *Cp* and Stanton number in Case 003 are similar to those of Case 002, both increasing first and then decreasing, but the fluctuations are less compared to the other two cases.

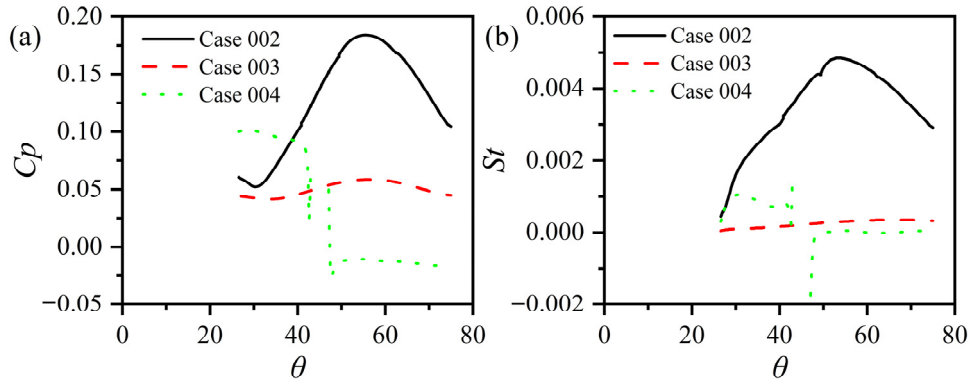


Figure 11. Comparison of (**a**) pressure coefficient and (**b**) Stanton number distributions on spike–single-zone jet configurations.

The bottom nozzle generates a characteristic under-expanded jet configuration, displaying an elongated morphology with extended penetration depth compared to the top and lateral jets. An upward-inclined shear layer, produced by the reattachment shock, generates an extensive recirculation region situated at the base of the aerospike and immediately downstream of the jet nozzle exit. This recirculation area exhibits markedly greater expansion compared to alternative jet arrangements. Both separation and reattachment shock structures are displaced away from the surface due to the influence of the high-speed jet effluent. As illustrated in Figure 10c, the freestream is effectively shielded from direct contact with the blunt body wall, as the jet envelops the frontal surface of the cone and extends over a section of the aerospike. From the distributions of the *Cp* and Stanton number of the blunt cone head in Figure 11, it can be observed that for the Case 004 configuration, when $\theta < 45^\circ$ and close to the spike, the wall pressure increases, and when $\theta > 45^\circ$ and away from the spike, the wall pressure decreases. The results indicate that the jet-induced wall coating elevates pressure on the side adjacent to the aerospike, displacing the reattachment shock further from the surface, while the jet's ejection effect reduces pressure on the opposite side. The calculated Stanton number of Case 004 is significantly lower than the results of Case 000 and Case 001.

3.3. Study on the Spike–Multi-Zone Jet Combined Configuration

Figure 12 displays Mach number and pressure contours for the combined aerospike and multi-zone jet configuration. Relative to the single-zone jet case, substantial alterations are observed in the flow field structure of the multi-zone jet arrangement. Firstly, the front end of the aerospike is only affected by the free stream and top jet, and the lateral jet and

the bottom jets do not affect the front-end flow field of the aerospike. In Case 003 and Case 005, alterations within the flow field remain relatively minor. This is attributed to the top jet generating only a limited recirculation region at the spike's tip, subsequently merging with the freestream and progressing downstream without inducing substantial changes to the flow further aft. A similarly modest discrepancy is observed between Case 004 and Case 006. Comparative analysis of Case 003, Case 004, Case 007, and Case 008 reveals that the synergistic interaction of the lateral and bottom jets promotes the development of an expanded recirculation zone situated between the spike base and the blunt cone. The configurations Case 007 and Case 008 displace the reattachment shock wave farther from the wall. Consequently, the Mach number of the fluid adjacent to the blunt cone surface is reduced, contributing positively to improved drag and heat flux reduction performance.

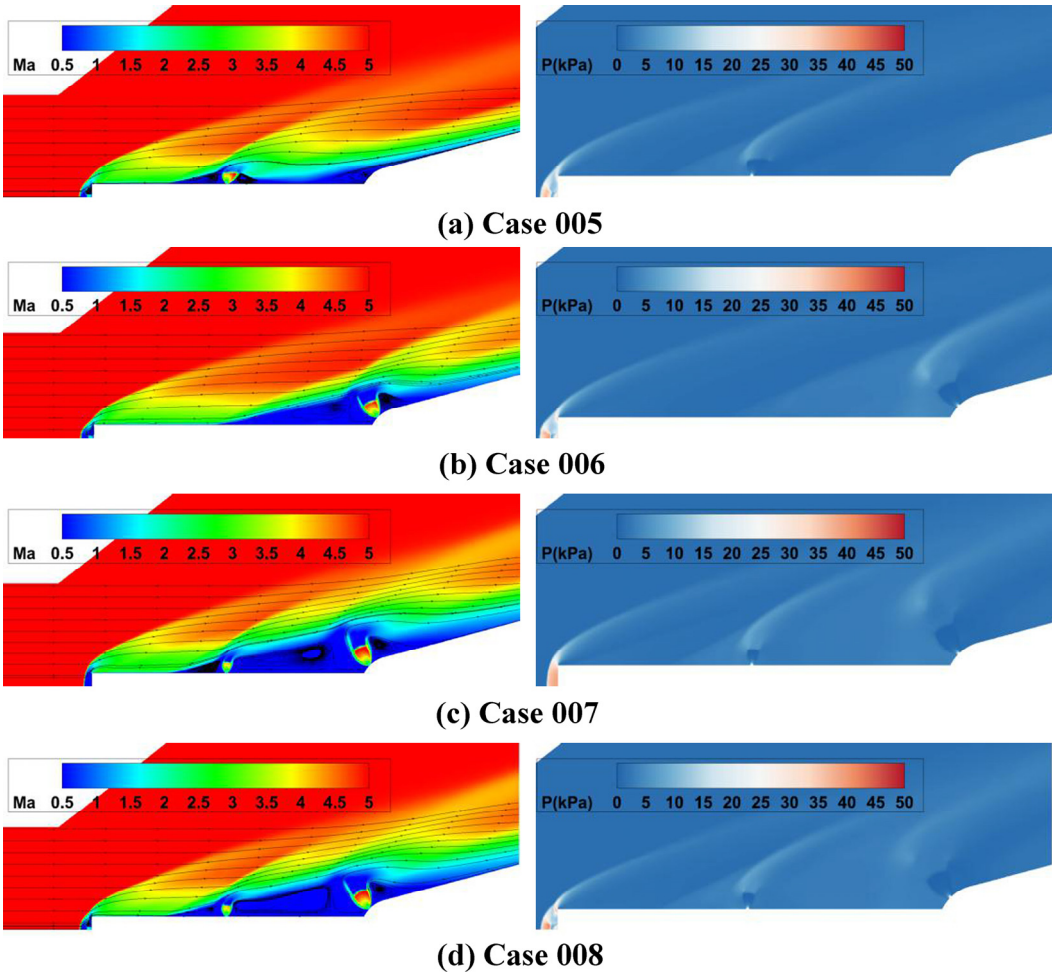


Figure 12. Mach numbers and pressure contours for (**a**) Case 005, (**b**) Case 006, (**c**) Case 007 and (**d**) Case 008.

Figure 13 illustrates the distributions of *Cp* and Stanton number across four distinct configurations. The outcomes reveal abrupt variations in both heat flux and pressure occurring at the jet nozzles. Owing to the influence of the jet emanating from the blunt body, at angles where $\theta < 45°$ and in regions proximate to the aerospike, the values of *Cp* and *St* exceed those observed in the configuration devoid of jet flow. When $\theta > 45°$ and in the direction away from the aerospike, the pattern is opposite. This implies that the wall jet, serving as the predominant factor, imposes a more substantial effect on thermal and pressure distributions relative to the reattachment shock wave. At locations distant from the jet nozzles, the variation trend of the Stanton number in Case 008 resembles that in

Case 007, yet the maximum Stanton number (St_{max}) is reduced, signifying that the design of Case 008 possesses a more effective heat reduction capability than both Case 006 and Case 007.

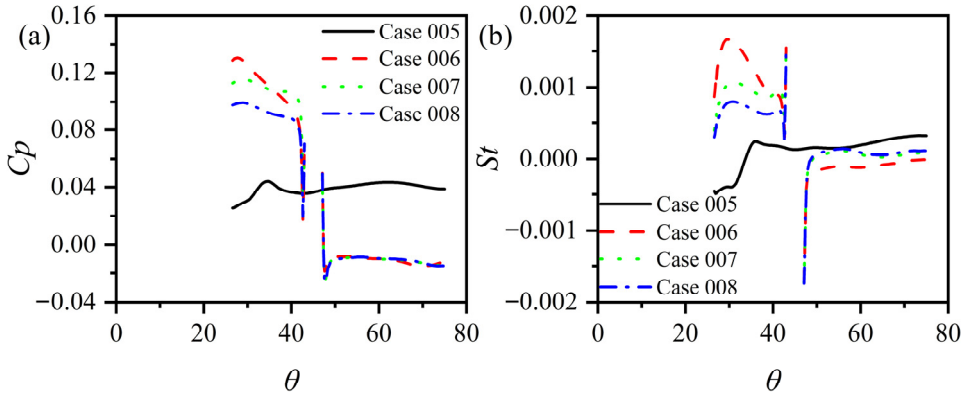


Figure 13. Comparison of (**a**) pressure coefficient and (**b**) Stanton number distributions of spike–multi-zone jet configurations.

3.4. Analysis of the Jet Effect

Figure 14 displays a comparative analysis of drag coefficients among various configurations. The incorporation of the aerospike and jet system yields markedly diminished drag relative to the baseline blunt cone. However, the achieved drag reduction proves less substantial than the reverse thrust produced by the top jet outflow, culminating in an aggregate drag marginally exceeding that observed in the absence of jet operation. Case 003 has no reverse force along the free flow direction; thus, the values of aerodynamic drag and total drag are the same. The results of Case 004 indicate that the bottom jet leads to a remarkable decrease in aerodynamic drag. Even considering the influence of the jet reverse force leading to a slightly increased actual drag compared with the aerodynamic drag, it is still smaller than the drag coefficients of Case 000 and Case 001. When considering solely the computation of aerodynamic drag, Case 008 exhibits the most effective drag reduction performance. The results of Case 006 and Case 007 are relatively close, while those of Case 005 are the worst. However, the multi-zone jet approach is confronted with the counterforce of simultaneous jets in different regions. The lateral jet generates a counterforce oriented perpendicularly to the direction of airflow. During drag calculation, the influence of this lateral jet mode can be disregarded, whereas the counterforces produced by the other two jet configurations must be accounted for. As established in prior analysis, the top jet exerts minimal influence on the downstream flow field. Consequently, the drag coefficients of Case 007 and Case 008 show little variation. The lateral jet contributes more significantly to drag reduction compared to the bottom jet. As a result, Case 005 demonstrates a lower drag coefficient than Case 006.

Furthermore, a quantitative assessment of jet efficiency is conducted using Equation (1), with computational outcomes illustrated in Figure 15. The drag and heat flux reduction achieved by the spike–top jet (Case 002) is less pronounced compared to the aerospike-only configuration. While both the jet applied along the spike and the blunt cone contribute to a reduction in the drag coefficient, the lateral jet configuration (Case 003) demonstrates superior performance to the bottom jet (Case 004), improving jet efficiency by 70%. The drag reduction efficiencies of all four multi-zone jet combined configurations (Case 005 through 008) are higher than that of the configuration without the spike. Among them, the configuration with the highest drag reduction efficiency is Case 008, reaching up to 230%.

Based on the preceding numerical simulation, Case 008 unquestionably exhibits the most effective drag and heat flux reduction and highest jet efficiency. However, due to

the constrained payload capacity of the high-speed vehicle, carrying a substantial mass of working fluid to enable drag and heat flux reduction and thermal management would contradict the fundamental objective of optimized system design. Therefore, the paper simultaneously evaluates the effects of the working medium's mass flow rate, the St_{max}, drag reduction efficiency, and the equivalent specific impulse. Corresponding data for various configurations are provided in Table 2. The top jet nozzle of the aerospike (Case 002) has the largest I, while the mass flow rate is the smallest. Cases 005–008 have multi-zone jets; thus, depending on the positions of the nozzles, the mass flow rates need to be calculated by superposition. The mass flow rate of Case 008 is undoubtedly the largest. It could be found from Figures 11 and 13 that the top jet configuration (Case 002) cannot reduce the St_{max}. Table 2 indicates that both adding the spike and the spike–jet configurations could diminish the heat flux across the surface. Among these, the lateral jet demonstrates the most pronounced effect, with Case 003 exhibiting the lowest St_{max}. When considering both mass flow rate and drag coefficient, the Case 003 configuration proves optimal for drag and heat flux reduction within the scope of this study.

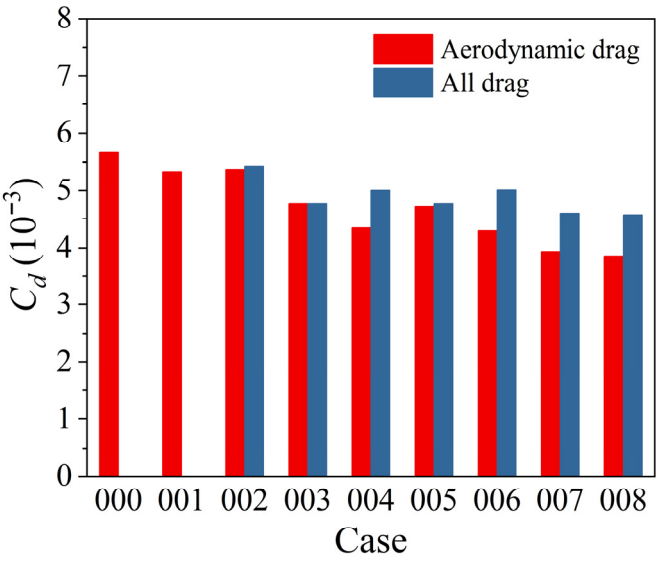


Figure 14. Comparison of drag coefficients for all cases.

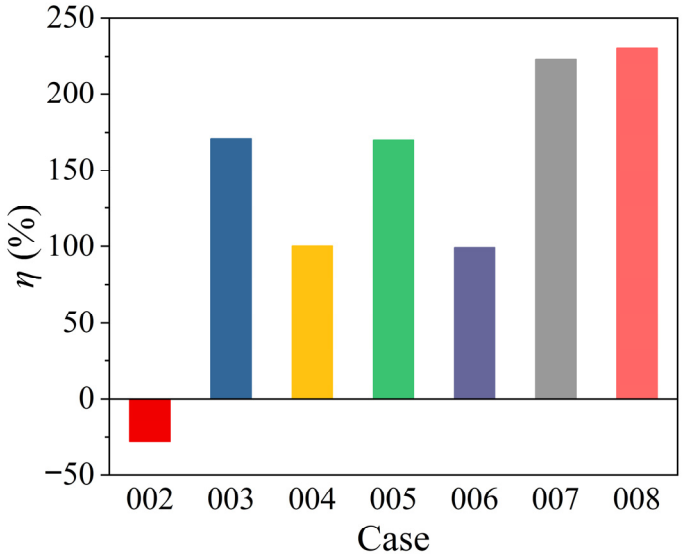


Figure 15. Comparison of jet efficiency for cases 002–008.

Table 2. Mass flow rate, maximum wall Stanton number, equivalent specific impulse and drag reduction efficiency for different cases.

Case	Q (kg/s)	St_{max} ($\times 10^{-3}$)	I (m/s)	η (%)
000	-	18.700	-	-
001	-	5.330	-	-
002	0.00381	4.850	2613.519	-28.035
003	0.02118	0.353	1769.245	170.651
004	0.03351	1.550	827.365	100.236
005	0.02499	0.323	1494.404	169.756
006	0.03732	1.670	738.742	99.130
007	0.05469	1.560	818.401	223.262
008	0.05851	1.550	782.213	230.506

4. Conclusions

This paper employs numerical simulation to investigate the complex flow field generated by the combined aerospike and jet configuration in a high-speed stream and examines how multi-zone jet injection influences drag and thermal load mitigation. The following conclusions are derived within the studied parameter range:

1. The computational methodology utilized in the paper proves suitable for simulating intricate high-speed flow fields, effectively capturing complex flow features including shock waves, shear layers, reattachment shocks, and recirculation zones. Both the incorporation of the aerospike and the implementation of jet injection significantly influence the structure of the flow field.
2. Within the combined flow field configuration comprising a spike and single-zone jet injection, both lateral and bottom jets effectively envelop the surfaces of the aerospike and blunt cone, thereby displacing the reattachment shock wave and separation shock wave away from the wall. Numerical simulation outcomes demonstrate that lateral and bottom jet flows are capable of concurrently attaining drag and heat flux reduction.
3. Within the combined flow field generated by the aerospike and multi-zone jet injection, downstream jet activity exerts no influence upon the upstream jet flow structure. The synergistic operation of lateral and bottom jets provides extensive coverage across the aerospike and blunt cone surface, establishing an enlarged recirculation zone enveloping the blunt cone's head and the aerospike's base. Numerical simulation outcomes reveal that the configuration integrating top and lateral jets delivers optimal thermal mitigation, and the Stmax is only 1/5 of that of other multi-zone jet schemes. The combined deployment of top, lateral, and bottom jets achieves superior drag reduction performance, and the drag reduction efficiency is up to 230.506%.
4. Considering the jet mass flow rate, the peak wall Stanton number, and the drag coefficient, the combined configuration of the spike and lateral jet demonstrates the optimal drag and heat flux reduction performance within the investigated parameter range. The equivalent specific impulse reaches 1769.245 m/s, and the drag reduction efficiency is 170.651%.

Author Contributions: Data curation, S.W.; conceptualization, Y.Z., H.T. and Z.T.; formal analysis, S.W., H.T. and Z.T.; investigation, S.W.; methodology, S.W., Y.Z. and H.T.; writing—original draft, S.W.; supervision, Y.Z. and Z.T.; writing—review &editing, Y.Z.; visualization, Z.T. All authors have read and agreed to the published version of the manuscript.

Funding: This research received no external funding.

Data Availability Statement: The data presented in this study are available on request from the corresponding author.

Conflicts of Interest: The authors declare no conflicts of interest.

References

1. Wang, Y.; Zhang, Q.; Tang, Z.; Tian, Z.; Zheng, Y. Integrated thermal protection system design for hypersonic vehicle based on new thermal-mechanical method. *J. Aerosp. Eng.* **2022**, *35*, 04021121. [CrossRef]
2. Cheng, J.; Chen, R.; Qiu, R.; Sun, W.; You, Y. Aerothermodynamic study of Two-Stage-To-Orbit system composed of wide-speed-range vehicle and rocket. *Acta Astronaut.* **2021**, *183*, 330–345. [CrossRef]
3. Shilwant, R.B.; Mahulikar, S.P. Aerothermal and aerodynamic characteristics of reusable hypersonic vehicles with heat transfer minimised sweepback. *Aeronaut. J.* **2024**, *128*, 2003–2022. [CrossRef]
4. Peters, A.B.; Zhang, D.; Chen, S.; Ott, C.; Oses, C.; Curtarolo, S.; McCue, I.; Pollock, T.M.; Eswarappa Prameela, S. Materials design for hypersonics. *Nat. Commun.* **2024**, *15*, 3328. [CrossRef] [PubMed]
5. Meng, Y.; Wang, Z.; Huang, W.; Niu, Y.; Yan, L. Coupled fluid–thermal analysis of the reduction mechanism for the drag and heat flux induced by jet interaction in a hypersonic reusable launch vehicle. *AIP Adv.* **2022**, *12*, 105124. [CrossRef]
6. Liu, Q.; Luo, Z.; Zhou, Y.; Xie, W.; Dong, S. On the drag reduction mechanism of hypersonic turbulent boundary layers subject to heated wall blowing. *Adv. Aerodyn.* **2023**, *5*, 7. [CrossRef]
7. Zhang, R.; Dong, M.; Huang, W.; Li, S.; Du, Z.; Liao, J. Drag and heat flux reduction mechanism induced by the combinational forward-facing cavity and pulsed counterflowing jet configuration in supersonic flows. *Acta Astronaut.* **2019**, *160*, 62–75. [CrossRef]
8. Ju, S.; Sun, Z.; Yang, G.; Prapamonthon, P.; Zhang, J. Parametric study on drag reduction with the combination of the upstream energy deposition and the opposing jet configuration in supersonic flows. *Acta Astronaut.* **2020**, *171*, 300–310. [CrossRef]
9. Xie, W.; Luo, Z.; Zhou, Y.; Xie, X.; Wu, J.; Bai, G.; Li, Z.; Dong, H.; Zhang, X. Experimental study on plasma synthetic jet for drag reduction in hypersonic flow. *AIAA J.* **2023**, *61*, 1428–1434. [CrossRef]
10. Esfeh, M.K.; Tajalli, S.M.; Liu, P. Evaluation of aerospike for drag reduction on a blunt nose using experimental and numerical modeling. *Acta Astronaut.* **2019**, *160*, 656–671. [CrossRef]
11. Camillo, G.P.; Wagner, A.; Dittert, C.; Benjamin, L.; Wartemann, V.; Neumann, J.; Hink, R. Experimental investigation of the effect of transpiration cooling on second mode instabilities in a hypersonic boundary layer. *Exp. Fluids* **2020**, *61*, 162. [CrossRef]
12. Lü, X.; Yuan, C.; Bao, W.; Bai, G.; Meng, F. Numerical and experimental investigation of aerodynamic heat control of leading edge of hypersonic vehicle's flexible skin. *Sci. China Inf. Sci.* **2022**, *65*, 202203. [CrossRef]
13. Hu, F.; Li, Z.; Wu, X.; Lin, W.; Zhang, J.; Jin, H.; Hu, Z. Numerical study for heat dissipation performance of phase transition cooling structure towards the wing antenna of hypersonic vehicle. *Appl. Therm. Eng.* **2024**, *245*, 122841. [CrossRef]
14. Wang, Z.; Zhang, X. Parametric research on drag reduction and thermal protection of blunt-body with opposing jets of forward convergent nozzle in supersonic flows. *Acta Astronaut.* **2022**, *190*, 218–230. [CrossRef]
15. Ni, Z.; Fang, S.; Guo, J.; Wang, Z. Research on drag reduction and heat prevention of hypersonic vehicle combined model with reverse jet and slot blowing. *J. Phys. Conf. Ser.* **2023**, *2459*, 12140. [CrossRef]
16. Jiang, Z.; Liu, Y.; Han, G.; Zhao, W. Experimental demonstration of a new concept of drag reduction and thermal protection for hypersonic vehicles. *Acta Mech. Sin.* **2009**, *25*, 417–419. [CrossRef]
17. Liu, Y.; Jiang, Z. Concept of non-ablative thermal protection system for hypersonic vehicles. *AIAA J.* **2013**, *51*, 584–590. [CrossRef]
18. Guo, J.; Fang, S.; Wang, Z.; Ni, Z.; Xu, Y. Investigation of drag and heat flux reduction induced by a novel combinational spike-aerodisk and channel concept for hypersonic blunt body. *Acta Astronaut.* **2023**, *204*, 207–221. [CrossRef]
19. Liu, T.; Fang, S.; Wang, Z.; Cheng, J. Drag reduction and thermal protection of the combination of aero disk, lateral jet, and rear jet for hypersonic vehicle. *J. Phys. Conf. Ser.* **2023**, *2636*, 12047. [CrossRef]
20. Ou, M.; Yan, L.; Huang, W.; Zhang, T. Design exploration of combinational spike and opposing jet concept in hypersonic flows based on CFD calculation and surrogate model. *Acta Astronaut.* **2019**, *155*, 287–301. [CrossRef]
21. Hayashi, K.; Aso, S.; Tani, Y. Experimental Study on Thermal Protection System by Opposing Jet in Supersonic Flow. *J. Spacecr. Rocket.* **2006**, *43*, 233–235. [CrossRef]
22. Motoyama, N.; Mihara, K.; Miyajima, R.; Watanuki, T.; Kubota, H. Thermal protection and drag reduction with use of spike in hypersonic flow. In Proceedings of the 10th AIAA/NAL-NASDA-ISAS International Space Planes and Hypersonic Systems and Technologies Conference, Kyoto, Japan, 24–27 April 2001. [CrossRef]

Disclaimer/Publisher's Note: The statements, opinions and data contained in all publications are solely those of the individual author(s) and contributor(s) and not of MDPI and/or the editor(s). MDPI and/or the editor(s) disclaim responsibility for any injury to people or property resulting from any ideas, methods, instructions or products referred to in the content.